Probabilistic Analysis of Power System Frequency Stability Considering Wake Effects of Wind Farms

Zhaoyuan Wang, *Graduate Student Member, IEEE* and Siqi Bu, *Senior Member, IEEE*

***Abstract*—Most existing studies on probabilistic frequency stability (PFS) affected by the uncertainty of wind power generation ignore the heterogeneity and interactions of wind turbines inside wind farms (WFs), i.e., wake effects (WEs), which will lead to inaccurate results. This paper proposes a method for analyzing PFS considering the WEs of WFs. Firstly, an analytical WE model suitable for PFS analysis is proposed. The proposed time-saving WE model can be easily integrated into the original frequency response model of power systems and comprehensively consider multiple types of terrains, the wind direction, and the time delay of wind flow, reflecting the WEs of WFs more realistically. To analyze the system frequency and the area-level frequency simultaneously and consider the implicit relationship between them, the multiple output Gaussian process regression is designed to improve efficiency and accuracy. Case studies are carried out to verify the effectiveness of the proposed method and demonstrate the necessity of considering the WEs of WFs in PFS analysis. Moreover, the impact of the wind direction, the terrain, and the layout on PFS is investigated.**

***Index Terms*—Analytical wake effect model, Gaussian process regression, probabilistic stability analysis, risk assessment, uncertainty propagation.**

I. Introduction

In response to energy shortages, many countries are vigorously developing wind power generation (WPG). However, the increasing penetration of WPG contributes to the decrease of power system inertia [1, 2], which would pose a huge threat to frequency stability (FS), even if there are WPG control schemes capable of providing system inertia. Moreover, the intermittence and the fluctuation of WPG have increased the risk of system power imbalance and further deteriorated FS [3]. Thus, it is crucial to investigate the impact of the uncertainties of WPG on FS of power systems with reduced inertia.

Commonly, probabilistic stability analysis includes two major tasks, i.e., uncertainty modeling and uncertainty propagation analysis. To model the generation uncertainties of wind farms (WFs), the basic idea is to apply the probability density functions (PDFs), cumulative density functions, or historical data to characterize the probability distribution of uncertainties of the wind speed [4] and then to model the relationship between the output power of WFs and the wind speed based on WF models. Moreover, in a WF, wind turbines (WTs) at the wind downstream position are affected by the wake of upstream WTs, resulting in the deficit of the downstream wind speed, i.e., wake effects (WEs). As summarized in existing studies [5, 6], WF models considering WEs mainly contain three types, i.e., the single-machine aggregated model (SAM), the multi-machine cluster-based aggregated model (MCAM), and the detailed model. Among them, SAMs use only one aggregated WT to characterize the WF and have the lowest accuracy. Normally, SAMs calculate the output power of every WT according to simplified maximum power point tracking (MPPT) and then derive the total output power of the WF. And finally, the aggregated wind speed is calculated by using the MPPT curve inversely [7]. Besides, authors in [8] have calculated the aggregated wind speed by directly averaging the wind speeds of all WTs. For MCAMs, the WF is characterized by multiple aggregated WTs with similar WE strength based on the cluster [5, 9, 10]. Moreover, in [11], the probabilistic cluster has been proposed to consider the uncertainty of wind. By comparison, the accuracy of both SAMs and MCAMs is lower than that of the detailed model, where all WTs with the corresponding wind speed are individually modeled without aggregation [12]. Thus, adopting the detailed WF model considering WEs to ensure the analysis accuracy is necessary. Additionally, in existing studies on probabilistic frequency stability (PFS) analysis, the applied WF models do not consider WEs [3, 13-15]. Thus, it is worth studying whether the ignorance of WEs is reasonable in PFS analysis based on the detailed WF model and what is the specific impact of WEs on PFS.

To characterize the WEs of WFs, different models have been proposed and can be mainly divided into numerical models and analytical models, which are summarized in some review papers [16-20]. Numerical WE models are based on computational fluid dynamics (CFD). According to the underlying turbulence modeling, CFD models can be categorized as the large eddy simulation and Reynolds-averaged Navier-Stokes [16]. The major merit of them is their high accuracy. However, they are quite time-consuming. To reduce time costs, actuator coupling, model simplification, and heterogeneous computing [21] are applied in CFD models.

Manuscript received xx xx, xxxx; revised xx xx, xxxx; accepted xx xx, xxxx. This work was supported in part by the National Natural Science Foundation of China for the Research Project under Grant 52077188, and in part by the Hong Kong Research Grant Council for the Research Project under Grants 15208323. (*Corresponding author: Siqi Bu.*)

Zhaoyuan Wang is with the Department of Electrical and Electronic Engineering, The Hong Kong Polytechnic University, Kowloon, Hong Kong, China. (e-mail: zhaoyuan.wang@connect.polyu.hk).

Siqi Bu is with Department of Electrical and Electronic Engineering, Shenzhen Research Institute, Research Centre for Grid Modernisation, International Centre of Urban Energy Nexus, Centre for Advances in Reliability and Safety, Research Institute for Smart Energy, and Policy Research Centre for Innovation and Technology, The Hong Kong Polytechnic University, Kowloon, Hong Kong. (e-mail: siqi.bu@polyu.edu.hk).

Color versions of one or more of the figures in this paper are available online at http://ieeexplore.ieee.org.

Digital Object Identifier xxxx

However, even if the acceleration manner is used, the computation still typically takes several hours [21]. Thus, time-consuming CFD models are not suitable for probabilistic stability analysis, where at least a few simulations are usually needed. By comparison, the significant merit of analytical WE models is that the computational time is quite limited. Hence, analytical WE models are more suitable for probabilistic stability analysis. Among the analytical WE models widely applied, the Jensen WE model is based on the principle of conservation of mass [12, 22]. The Frandsen WE model is based on the principle of conservation of mass and momentum [23]. However, these two WE models assume that the wind speed at the same streamwise section in the wake region is identical, which is not in line with actual WEs. In fact, the shape of the wind speed deficit due to WEs is more similar to the Gaussian function [16]. Thus, to improve the accuracy of WEs, the Gaussian WE model is proposed [24]. Moreover, some improved analytical WE models have been proposed to consider the impact of different factors on WEs, including the wind direction [5, 9-11, 25], the single complex terrain [25, 26], and the time delay of wind flow [27]. However, these existing studies only consider the above factors partly rather than entirely and only consider one type of complex terrain rather than multiple types. Moreover, most of the existing analytical WE models considering different factors are based on the Jensen WE model [5, 9-12, 25, 26], the accuracy of which is limited. Thus, an accurate WE model suitable for PFS analysis and comprehensively considering the multiple factors affecting the WEs of WFs is required.

Additionally, uncertainty propagation analysis mainly consists of three approaches, i.e., numerical approaches, analytical approaches, and approximation approaches. One of the most typical numerical approaches is Monte Carlo simulation (MCS) [4], the results of which are usually regarded as the baseline to verify the performance of other methods. Besides, some methods for improving the sampling efficiency are proposed, e.g., Latin hypercube sampling (LHS) and quasi-MCS [28]. However, the time-consuming characteristic restricts the wide application of them in practice. Analytical approaches mainly include cumulant-based methods [13] and point estimation methods [29]. Cumulant-based methods utilize the cumulant of uncertainties to estimate that of concerned system responses and apply the series expansion to estimate the PDFs of concerned system responses. By comparison, point estimation methods utilize the central moment. However, the accuracy of estimated PDFs by analytical approaches is limited [30, 31].

For approximation approaches, polynomial chaos expansion (PCE) [32, 33] and low-rank approximation (LRA) [34] are two typical methods based on orthogonal polynomials corresponding to the probability distributions of uncertainties. PCE is in the extended form. LRA is in the tensor-product form. However, the explicit correlation expression of uncertainties is required for PCE, LRA, and analytical approaches. Furthermore, the complicated correlation induced by WEs cannot be characterized as expected. Thus, they are not suitable for probabilistic stability analysis considering WEs. Recently, another approximation approach, i.e., Gaussian process regression (GPR), has been applied to probabilistic stability analysis of power systems, including voltage stability [28] and transient stability [35]. Thanks to the merit of GPR that only the sampling points of uncertainties are needed [36], GPR has the potential to analyze the probabilistic stability considering WEs. However, to the best of our knowledge, there is no attempt at PFS analysis by applying GPR and considering WEs. Moreover, both the system frequency and the area-level frequency are concerned in PFS, and there is an implicit relationship between the system and area-level frequency responses. If the conventional GPR with only one output is applied to analyze the probabilistic stability of system and area-level frequency responses individually, the implicit relationship will be overlooked. Therefore, to improve analysis accuracy, a GPR with multiple outputs considering the relationship between frequency responses is required.

In view of the aforementioned background, a PFS analysis method considering the WEs of WFs is proposed in this paper. The main contributions of the paper are summarized as follows.

1) The designed multiple output GPR (MOGPR) analyzes the probabilistic stability of the system frequency and the area-level frequency simultaneously and considers the relationship between them, which improves the analysis accuracy and efficiency. These PFS analysis results will provide guidance to equip additional frequency regulation control. Furthermore, since GPR-based methods only require the sampling points of uncertainties, both MOGPR and GPR are suitable for the correlation caused by WEs. By comparison, the existing PCE and LRA cannot handle it.
2) The necessity of considering the WEs of WFs in PFS analysis is revealed based on the proposed WE model, which is ignored in the existing studies. This model possesses many merits: a) It only brings a slight increase in terms of the computational time when considering WEs of WFs in PFS analysis; b) Based on the Gaussian WE model, it comprehensively considers multiple types of terrains, the wind direction, and the time delay of wind flow, which can be applied to study the impact of different factors on PFS; c) It can be easily integrated into the original frequency response models of power systems ignoring WEs without modifications. Thus, it is suitable for PFS analysis and realistically reflects the WEs in WFs.
3) The impact of the wind direction, the terrain, and the WT layout on PFS is investigated. These factors will result in different wind speed deficits caused by different WEs, the levels of nature wind speeds, and WPG penetrations, thereby affecting PFS. The results will provide guidance to plan the WF siting and layout considering PFS.

The remaining sections are organized as follows. In Section II, a WE model of WF considering multiple factors is proposed. In addition, the system and area-level frequency responses are given. Section III designs MOGPR for PFS analysis to improve the accuracy and the efficiency. In Section IV, the case study is conducted to verify the effectiveness of the proposed method and study the impact of different factors on PFS. Section V

draws the conclusions.

II. Wake Effect Model of the Wind Farm Considering Multiple Factors for Analyzing Frequency Responses

A. Wake Effect Model of the Wind Farm Considering Multiple Factors

1) Basic WE Model

The WE of the WT based on the Gaussian model is shown in Fig. 1.

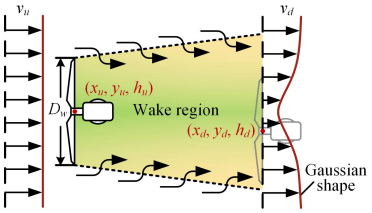

Fig. 1. WE of the WT based on the Gaussian WE model.

In Fig. 1, v_u is the incoming upstream wind speed. v_d is the downstream wind speed in the wind direction, which is lower than v_u due to the WE of the WT. (x_u, y_u, h_u) and (x_d, y_d, h_d) are the positions of the upstream and indicated downstream WTs separately. D_w is the diameter of the upstream WT blade.

According to the mass and momentum conservation,

$$\int \rho v_u (v_u - v_d) dS = C_T \rho S_w v_u^2 / 2, \tag{1}$$

where ρ is the air density. S denotes the cross-sectional area of the wake. C_T is the thrust coefficient of the WT. S_w denotes the area swept by the WT blades, which has the following relationship with the cross-sectional area of the wake just after the initial wake expansion S_0 [24]:

$$S_w = \alpha S_0, \tag{2}$$

where $\alpha = (1+\sqrt{1-C_T}) / (2\sqrt{1-C_T})$.

The Gaussian WE model assumes that the wind speed deficit has a Gaussian shape [24]. Thus, the normalized downstream wind speed deficit d_w can be expressed as:

$$d_w = (v_u - v_d) / v_u = g(x_d - x_u) e^{-\lambda}, \tag{3}$$

where $\lambda = [(y_d - y_u)^2 + (h_d - h_u)^2] / (2D_w^2 \sigma_w^2)$. σ_w denotes the width of the wake. $g(.)$ is the function of the wind speed deficit at the center of the wake region.

Thus, the downstream wind speed v_d can be expressed as:

$$v_d = [1 - g(x_d - x_u) e^{-\lambda}] v_u. \tag{4}$$

Substituting (4) into (1),

$$8(\sigma_w / D_w)^2 g(x_d - x_u)^2 - 16(\sigma_w / D_w)^2 g(x_d - x_u) + C_T = 0. \tag{5}$$

Solving (5) and taking the solution in line with the actual situation, $g(.)$ can be derived as:

$$g(x_d - x_u) = 1 - \sqrt{1 - C_T / [8(\sigma_w / D_w)^2]}. \tag{6}$$

Usually, the wake region is regarded as the linear expansion. Thus, σ_w / D_w can be expressed as:

$$\sigma_w / D_w = k_w (x_d - x_u) + \varepsilon_w, \tag{7}$$

where k_w is the wake region growth rate. $\varepsilon_w = 0.25\sqrt{\alpha}$ [24].

Substituting (6) and (7) into (4), v_d can be derived as:

$$v_d = [1 - (1 - \sqrt{1 - C_T / \{8[k_w (x_d - x_u) + \varepsilon_w]^2\}}) e^{-\lambda}] v_u. \tag{8}$$

2) Considering Terrain

In the basic Gaussian WE model, the impact of the terrain is ignored. According to the Lissaman model [26], the nature wind speed varies at different heights, which can be described as:

$$v'_{dn} / v_u = (h_d / h_u)^{\gamma}, \tag{9}$$

where v'_{dn} is the nature wind speed at the height h_d ignoring the terrain. γ is the coefficient of the wind speed variation with the height.

In addition, according to the lossless Bernoulli equation, the relationship between the wind speed deficits corresponding to different wind speeds can be described as [25]:

$$d_w / d_{wn} = (v'_{dn} / v_u)^2, \tag{10}$$

where d_{wn} is the normalized wind speed deficit corresponding to v'_{dn}.

After considering the airflow of different terrains, the nature wind speed v_{dn} at the height h_d can be expressed as [37]:

$$v_{dn} = (1 + c_1 H / L e^{-c_2 h_d / L}) v'_{dn}, \tag{11}$$

where H and L are the height and length of the terrain, respectively. c_1 and c_2 are the airflow coefficients of different terrains.

Apart from the flat terrain, three complex terrains are included in this WE model, which can be formulated as [37]:

$$h_c = \begin{cases} H / (1 + x_c^2 / L^2), \text{ Ridge} \\ H e^{-\ln 2[x_c^2 + y_c^2]/L^2}, \text{ Circular hill} \\ H[1 + \cos(\pi \sqrt{x_c^2 + y_c^2} / (2L))] / 2, \text{ Rolling terrain} \end{cases}, \tag{12}$$

where (x_c, y_c, h_c) is a relative position from the terrain center.

Substituting (9)-(12) into (8), the WE considering the terrain can be expressed as:

$$v_d = [1 - (1 - \sqrt{1 - C_T / \{8[k_w (x_d - x_u) + \varepsilon_w]^2\}}) \cdot e^{-\lambda} (h_u / h_d)^{2\gamma}] (h_d / h_u)^{\gamma} v_u. \tag{13}$$

3) Considering Wind Direction

When the wind direction changes, the relative position of the WT changes, which may cause the original upstream WT to become a downstream WT. Therefore, it is necessary to convert the relative position of the WT from its geographical location to its relative position along the wind direction. Assume that the angle between the wind direction and the positive direction of the x-axis on the x-y plane is θ_{xy}, and the angle between the wind direction and the positive direction of the y-axis on the y-h plane is θ_{yh}. The conversion between the position of WTs in the wind speed coordinate system (x_w, y_w, h_w) and the position in the geographic coordinate system $(x_.\, y_.\, h_.)$ is [12]:

$$(x_w, y_w, h_w) = (x_., y_., h_.) T_{yh} T_{xy}, \tag{14}$$

where $T_{yh} = \begin{bmatrix} 1 & 0 & 0 \\ 0 & \cos\theta_{yh} & \sin\theta_{yh} \\ 0 & -\sin\theta_{yh} & \cos\theta_{yh} \end{bmatrix}$. $T_{xy} = \begin{bmatrix} \cos\theta_{xy} & \sin\theta_{xy} & 0 \\ -\sin\theta_{xy} & \cos\theta_{xy} & 0 \\ 0 & 0 & 1 \end{bmatrix}$.

Substituting (14) into (13), the WE considering the wind direction can be derived as:

$$v_d = [1 - (1 - \sqrt{1 - C_T / \{8[k_w (x_{dw} - x_{uw}) + \varepsilon_w]^2\}}) \cdot e^{-\lambda_w} (h_u / h_d)^{2\gamma}] (h_d / h_u)^{\gamma} v_u, \tag{15}$$

where λ_w is λ calculated in the wind speed coordinate system.

4) **Considering the WEs of Multiple Upstream Wind Turbines**

The above WE model only considers the WE of one upstream WT on the wind speed of the downstream WT. In reality, all upstream WTs affect the downstream wind speed, and the downstream wind speed deficit is the superposition of the WEs of all upstream WTs, which can be described as [9]:

$$v_d = v_{dn}(1-\sqrt{\sum_{j=1}^{N_u} d_{wj}^2}), \tag{16}$$

where N_u is the quantity of upstream WTs.

Substituting (15) into (16), the WEs considering multiple upstream WTs can be derived as:

$$v_d = v_{dn} - \sqrt{\sum_{j=1}^{N_u} \{[(1-\sqrt{1-C_T / \{8[k_w(x_{dw}-x_{uwj})+\varepsilon_w]^2\}})\cdot e^{-\lambda_{wj}}(h_{uj}/h_d)^{2\gamma}](h_d/h_{uj})^{\gamma} v_{uj}\}^2}, \tag{17}$$

where λ_{wj} is λ_w of j-th upstream WT.

5) **Considering the Time Delay of Wind Flow**

Since WFs usually cover large geographic areas, it may take an unignorable time period for the wind to pass through WFs. If there is a wind speed change at the time t from the upstream position, the downstream wind speed $v_d(t)$ will change correspondingly after a time delay τ rather than simultaneously. Thus, $v_d(t)$ is calculated based on the wind speed at $t-\tau$, and the time delay can be determined by the integral of the downstream distance divided by the wind speed, i.e., $\tau = \int_0^{x_{dw}} 1/v_d dx$ [12]. Thus, after considering the time delay of wind flow and WEs, the wind speed can be expressed as:

$$v_d(t) = v_{dn}(t-\tau) - \sqrt{\sum_{j=1}^{N_u} \{[(1-\sqrt{1-C_T / \{8[k_w(x_{dw}-x_{uwj})+\varepsilon_w]^2\}})\cdot e^{-\lambda_{wj}}(\frac{h_{uj}}{h_d})^{2\gamma}](\frac{h_d}{h_{uj}})^{\gamma} v_{uj}(t-\tau)\}^2}. \tag{18}$$

B. System and Area-Level Frequency Responses

In this paper, WTs adopt permanent magnet synchronous generators (PMSGs) as examples [38]. The power electronic-interfaced PMSG includes three parts: the PMSG, the machine side converter (MSC), and the grid side converter (GSC) [39], as presented in Fig. 2 (a). MSC and GSC controllers are shown in Fig. 2 (b), where the droop control is flexibly equipped as the additional frequency regulation control for WTs. In addition, the primary frequency regulation for synchronous generators (SGs) and automatic generation control (AGC) are considered [40], as shown in Fig. 2 (c). The area-level frequency is determined by the frequency of SGs within the area, which can be calculated as [15]:

$$f_{ai} = \sum_{q=1}^{N_g} H_{sq} f_{sq} / \sum_{q=1}^{N_g} H_{sq}, \tag{19}$$

where f_{ai} is the frequency of the i-th area. N_g denotes the quantity of SGs in the i-th area. H_{sq} and f_{sq} are the inertia and frequency of the q-th SG, respectively.

From Fig. 2, the variation of the nature wind speed will change the received wind speed of WTs in WFs in different degrees due to WEs, which will lead to the output power variations of WTs according to MPPT. Thus, the power imbalance will occur and result in the speed regulation of SGs, thereby affecting the frequency. Similarly, the system frequency f_{sys} is determined by the area-level frequency, which can be calculated as:

$$f_{sys} = \sum_{i=1}^{N_a} H_{ai} f_{ai} / \sum_{i=1}^{N_a} H_{ai}, \tag{20}$$

where N_a denotes the quantity of areas. H_{ai} and f_{ai} are the inertia and frequency of the i-th area, respectively.

Additionally, from Fig. 2, the proposed WE model and the frequency response of power systems are calculated individually, where the WE model outputs are the inputs of the power system model. Thus, this WE model can be easily integrated into PFS analysis without any modifications to the power system model ignoring WEs.

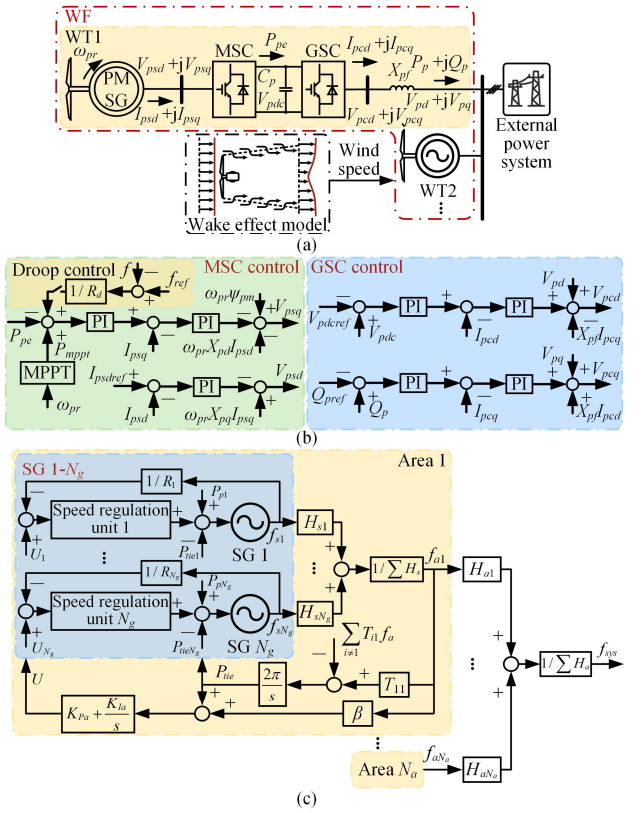

Fig. 2. (a) WF model; (b) WT control strategy; (c) System and area-level frequency responses.

III. Multiple Output Gaussian Process Regression for Probabilistic Frequency Stability Analysis

A. Multiple Output Gaussian Process Regression (MOGPR)

GPR-based uncertainty propagation analysis adopts a reduced model $\mathcal{M}(.)$ to describe the relationship between the sampling point of uncertainties $\boldsymbol{\xi} = \{\xi_{lr}\}$ and the observation points of the concerned system response $\boldsymbol{z} = \{z_{br}\}$, where ξ_{lr} is the r-th sampling point of l-th uncertainty, and z_{br} is the r-th observation point of b-th output, where $b=1$ in conventional GPR. In this paper, $\boldsymbol{\xi}$ is the wind speed, $\boldsymbol{z}$ is the FS index.

Thus, GPR-based method can be formulated as:

$$z \approx \hat{z} = \mathcal{M}(\boldsymbol{\xi}) + \boldsymbol{\varepsilon}, \tag{21}$$

where superscript ^ denotes the estimated output by GPR-based method. $\boldsymbol{\varepsilon}$ is the error from the observation of z, which follows Gaussian distribution $\boldsymbol{\varepsilon} \sim \mathcal{N}(\mathbf{0}, \sigma_\varepsilon^2 \boldsymbol{I})$ with the standard deviation of σ_ε. $\boldsymbol{I}$ is the identity matrix. $\mathcal{M}(\boldsymbol{\xi})$ is the Gaussian process (GP) defined by the mean m and the covariance kernel function $\hat{k}(\boldsymbol{\xi}, \boldsymbol{\xi}; \boldsymbol{\theta})$ as [35]:

$$\mathcal{M}(\boldsymbol{\xi}) \sim \mathcal{GP}(m, \hat{k}(\boldsymbol{\xi}, \boldsymbol{\xi}; \boldsymbol{\theta})), \tag{22}$$

where $\boldsymbol{\theta}$ denotes the parameter vector of the kernel function.

It should be noted that GP is used to characterize the sampling points of uncertainties and the observation points of the corresponding FS index rather than uncertainties and corresponding FS index themselves, as presented in (22). Thus, GPR does not require that uncertainties and corresponding FS index have to follow Gaussian distributions and is suitable for arbitrary distributions. It can be seen in (21) that conventional GPR has only one output. However, both the system frequency and the area-level frequency are concerned and need to be analyzed in PFS. If conventional GPR is applied to analyze them, multiple GPR models will be built, which is time-consuming. Moreover, there are implicit relationships between system and area-level frequency responses. One of the obvious relationships is that the system frequency is the weighted average of the area-level frequency, as shown in (20). However, building individual GPR models will not consider these relationships and may lead to inaccurate PFS analysis results. Thus, to quantify the probabilistic system and area-level frequency responses simultaneously and characterize the implicit relationships between them, thereby improving accuracy and efficiency, MOGPR suitable for PFS analysis is designed.

1) **Model Construction of MOGPR**

Motivated by the combination relationship of the frequency presented in (20), N_o outputs $\boldsymbol{\mathcal{M}}(\boldsymbol{\xi}) = [\mathcal{M}_1(\boldsymbol{\xi}), \cdots, \mathcal{M}_{N_o}(\boldsymbol{\xi})]^T$ are designed similarly to be formed by the combination of N_l latent factors $\boldsymbol{u}(\boldsymbol{\xi}) = [u_1(\boldsymbol{\xi}), \cdots, u_{N_l}(\boldsymbol{\xi})]^T \sim \mathcal{GP}(\boldsymbol{m}, \hat{\boldsymbol{k}}(\boldsymbol{\xi}, \boldsymbol{\xi}; \boldsymbol{\theta}))$ modeled by GP as [41]:

$$\begin{bmatrix} \mathcal{M}_1(\boldsymbol{\xi}) \\ \vdots \\ \mathcal{M}_{N_o}(\boldsymbol{\xi}) \end{bmatrix} = \begin{bmatrix} a_{11} & \cdots & a_{1N_l} \\ \vdots & \ddots & \vdots \\ a_{N_o 1} & \cdots & a_{N_o N_l} \end{bmatrix} \begin{bmatrix} u_1(\boldsymbol{\xi}) \\ \vdots \\ u_{N_l}(\boldsymbol{\xi}) \end{bmatrix}, \tag{23}$$

where $a_{\cdot}$ is the element of coefficient matrix $\boldsymbol{A}$.

From (23), the connection of all outputs is established by the introduction of $\boldsymbol{u}(\boldsymbol{\xi})$. The implicit relationship among outputs is reflected in $\boldsymbol{A}$. Thus, the proposed method for PFS analysis can reflect the relationship between the system frequency and the area-level frequency. Applying $\boldsymbol{a_n} = [a_{1n}, \cdots, a_{N_o n}]^T$ to represent the n-th column vector of $\boldsymbol{A}$, the covariance of outputs can be calculated as:

$$\begin{aligned} \boldsymbol{C}(\boldsymbol{\xi}, \boldsymbol{\xi}) &= \mathbf{E}[\boldsymbol{\mathcal{M}}(\boldsymbol{\xi})\boldsymbol{\mathcal{M}}(\boldsymbol{\xi})^T] - \mathbf{E}[\boldsymbol{\mathcal{M}}(\boldsymbol{\xi})]\mathbf{E}^T[\boldsymbol{\mathcal{M}}(\boldsymbol{\xi})] \\ &= \sum_{n=1}^{N_l} \boldsymbol{a_n}\boldsymbol{a_n}^T \otimes \{\mathbf{E}[u_n(\boldsymbol{\xi})u_n(\boldsymbol{\xi})] - \mathbf{E}[u_n(\boldsymbol{\xi})]\mathbf{E}[u_n(\boldsymbol{\xi})]\} \\ &= \boldsymbol{A}\boldsymbol{A}^T \otimes \hat{\boldsymbol{k}}(\boldsymbol{\xi}, \boldsymbol{\xi}; \boldsymbol{\theta}), \end{aligned} \tag{24}$$

where $\mathbf{E}[.]$ is the mean operator. $\otimes$ denotes the operator of the Kronecker product.

Thus, the joint prior distribution of the observed system outputs $\boldsymbol{Z}_s$ corresponding to the sampling points of uncertainties $\boldsymbol{\xi}_s$ and $\boldsymbol{\mathcal{M}}(\boldsymbol{\xi}_e)$ corresponding to the points of uncertainties to be analyzed $\boldsymbol{\xi}_e$ is:

$$\begin{bmatrix} \boldsymbol{Z}_s \\ \boldsymbol{\mathcal{M}}(\boldsymbol{\xi}_e) \end{bmatrix} \sim \mathcal{N}\left(\begin{bmatrix} \boldsymbol{m}_s \\ \boldsymbol{m}_e \end{bmatrix}, \begin{bmatrix} \boldsymbol{A}\boldsymbol{A}^T \otimes \boldsymbol{\mathcal{K}}_{ss} + \sigma_\varepsilon^2 \boldsymbol{I} & \boldsymbol{A}\boldsymbol{A}^T \otimes \boldsymbol{\mathcal{K}}_{se} \\ \boldsymbol{A}\boldsymbol{A}^T \otimes \boldsymbol{\mathcal{K}}_{es} & \boldsymbol{A}\boldsymbol{A}^T \otimes \boldsymbol{\mathcal{K}}_{ee} \end{bmatrix} \right), \tag{25}$$

where $\boldsymbol{m}_s$ and $\boldsymbol{m}_e$ are the means corresponding to $\boldsymbol{\mathcal{M}}(\boldsymbol{\xi}_s)$ and $\boldsymbol{\mathcal{M}}(\boldsymbol{\xi}_e)$ respectively. $\boldsymbol{\mathcal{K}}_{se}$ denotes $\hat{\boldsymbol{k}}(\boldsymbol{\xi}_s, \boldsymbol{\xi}_e; \boldsymbol{\theta})$.

Thus, the posterior mean $\boldsymbol{m}_{pe}$ and the covariance $\boldsymbol{\mathcal{K}}_{pe}$ of $\boldsymbol{\mathcal{M}}(\boldsymbol{\xi}_e)$ can be derived as:

$$\begin{cases} \boldsymbol{m}_{pe} = \boldsymbol{m}_e + (\boldsymbol{A}\boldsymbol{A}^T \otimes \boldsymbol{\mathcal{K}}_{es}) \cdot \\ \qquad (\boldsymbol{A}\boldsymbol{A}^T \otimes \boldsymbol{\mathcal{K}}_{ee} + \sigma_\varepsilon^2 \boldsymbol{I})^{-1} (\boldsymbol{Z}_s - \boldsymbol{m}_s) \\ \boldsymbol{\mathcal{K}}_{pe} = \boldsymbol{\mathcal{K}}_{ee} - (\boldsymbol{A}\boldsymbol{A}^T \otimes \boldsymbol{\mathcal{K}}_{es}) \cdot \\ \qquad (\boldsymbol{A}\boldsymbol{A}^T \otimes \boldsymbol{\mathcal{K}}_{ee} + \sigma_\varepsilon^2 \boldsymbol{I})^{-1} (\boldsymbol{A}\boldsymbol{A}^T \otimes \boldsymbol{\mathcal{K}}_{se}) \end{cases}. \tag{26}$$

2) **Calculation of Undetermined Coefficients**

According to (26), $\boldsymbol{\theta}$ and $\boldsymbol{A}$ are undetermined and to be calculated.

According to the Bayesian theorem,

$$p(\boldsymbol{\theta}, \boldsymbol{A} \mid \boldsymbol{Z}_s, \boldsymbol{\xi}_s) = p(\boldsymbol{Z}_s \mid \boldsymbol{\xi}_s, \boldsymbol{\theta}, \boldsymbol{A})\, p(\boldsymbol{\theta}, \boldsymbol{A}) / p(\boldsymbol{Z}_s \mid \boldsymbol{\xi}_s), \tag{27}$$

where $p(\boldsymbol{\theta}, \boldsymbol{A} \mid \boldsymbol{Z}_s, \boldsymbol{\xi}_s)$ is the posterior probability of $\boldsymbol{\theta}$ and $\boldsymbol{A}$. $p(\boldsymbol{Z}_s \mid \boldsymbol{\xi}_s, \boldsymbol{\theta}, \boldsymbol{A})$ denotes the likelihood function. $p(\boldsymbol{\theta}, \boldsymbol{A})$ is the prior probability of $\boldsymbol{\theta}$ and $\boldsymbol{A}$. $p(\boldsymbol{Z}_s \mid \boldsymbol{\xi}_s)$ denotes the evidence.

The optimization of $\boldsymbol{\theta}$ and $\boldsymbol{A}$ is equivalent to maximizing $p(\boldsymbol{\theta}, \boldsymbol{A} \mid \boldsymbol{Z}_s, \boldsymbol{\xi}_s)$, i.e., maximum likelihood estimation. Since $p(\boldsymbol{Z}_s \mid \boldsymbol{\xi}_s)$ is fixed when $\boldsymbol{Z}_s$ and $\boldsymbol{\xi}_s$ are given, and $p(\boldsymbol{\theta}, \boldsymbol{A})$ is known in advance, $p(\boldsymbol{\theta}, \boldsymbol{A} \mid \boldsymbol{Z}_s, \boldsymbol{\xi}_s)$ is proportional to $p(\boldsymbol{Z}_s \mid \boldsymbol{\xi}_s, \boldsymbol{\theta}, \boldsymbol{A})$. For the convenience of calculation, the optimization objective $\mathcal{L}$ is transformed into minimizing the $-\log p(\boldsymbol{Z}_s \mid \boldsymbol{\xi}_s, \boldsymbol{\theta}, \boldsymbol{A})$ as:

$$\begin{aligned} \mathcal{L} &= -\log p(\boldsymbol{Z}_s \mid \boldsymbol{\xi}_s, \boldsymbol{\theta}, \boldsymbol{A}) \\ &= \boldsymbol{Z}_s^T (\boldsymbol{A}\boldsymbol{A}^T \otimes \boldsymbol{\mathcal{K}}_{ee} + \sigma_\varepsilon^2 \boldsymbol{I}) \boldsymbol{Z}_s / 2 \\ &\quad + \log | \boldsymbol{A}\boldsymbol{A}^T \otimes \boldsymbol{\mathcal{K}}_{ee} + \sigma_\varepsilon^2 \boldsymbol{I} | /2 + N_s \log 2\pi / 2, \end{aligned} \tag{28}$$

where N_s is the quantity of sampling points $\boldsymbol{\xi}_s$.

In summary, MOGPR $\boldsymbol{\mathcal{M}}(\boldsymbol{\xi}; \boldsymbol{\theta}, \boldsymbol{A})$ approximates the relationship between uncertainties and FS indices with the sampling points of uncertainties as inputs and those of FS indices as outputs in the form of (25), which is a regression task. To calculate the undetermined coefficients $\boldsymbol{\theta}$ and $\boldsymbol{A}$ in (25), maximum likelihood estimation is adopted, which can be transformed into minimizing (28). After $\boldsymbol{\theta}$ and $\boldsymbol{A}$ are calculated, MOGPR can be used to estimate FS indices corresponding to the points of uncertainties to be analyzed $\boldsymbol{\xi}_e$, which are $\boldsymbol{\mathcal{M}}(\boldsymbol{\xi}_e; \boldsymbol{\theta}, \boldsymbol{A})$ with the highest probabilities, i.e., $\boldsymbol{m}_{pe}$, in the form of (26). Additionally, in this paper, L-BFGS is used to solve (28). Moreover, to improve the sampling efficiency, LHS [35] is applied to acquire $\boldsymbol{\xi}_s$.

B. Probabilistic Frequency Stability Analysis

FS refers to the ability of power systems to maintain the frequency, i.e., synchronism, and mitigate the frequency

deviation [4, 42]. Hence, the frequency response, including the rate of change of frequency (RoCoF) and the frequency nadir/vertex (FN/FV), are the main FS indices [4, 43], which are considered in this paper. RoCoF FSI_R and FN/FV FSI_F can be described as:

$$\begin{cases} FSI_R = \min/\max(df/dt) \\ FSI_F = \min/\max(f) \end{cases}, \tag{29}$$

where f is the frequency.

After MOGPR is constructed, the data of estimated FS indices $\boldsymbol{m}_{pe}$ can be directly calculated according to (26) when the system is under the uncertainties with the sampling points $\boldsymbol{\xi}_s$. To estimate the closed-form PDFs of FS indices based on the data $\boldsymbol{m}_{pe}$, kernel density estimation (KDE) [35] is adopted, which is a nonparametric method using the kernels corresponding to data as components to form PDFs and can be formulated as:

$$p_{\hat{z}_b}(\hat{z}_b) = \sum_{r=1}^{N_e} p_K[(\hat{z}_b - m_{pebr})/\delta_{Kb}]/(N_e\delta_{Kb}), \tag{30}$$

where N_e is the quantity of data $\boldsymbol{\xi}_e$. m_{pebr} denotes the r-th sampling point of $\boldsymbol{m}_{pe}$ corresponding to b-th output. $p_K[.]$ denotes the kernel function of KDE, which is selected as the Gaussian kernel, i.e., $p_K[(\hat{z}_b - m_{pebr})/\delta_{Kb}] = e^{-(\hat{z}_b - m_{pebr})^2/(2\delta_{Kb}^2)}$. δ_{Kb} is the bandwidth of kernels.

Moreover, apart from PDFs, the risk assessment matrix (RAM) [13] is also concerned in PFS analysis, which is used to assess the occurrence probability of the frequency instability risk. In this paper, FS risk regions are partitioned as 'Low Risk', 'Medium Risk', and 'High Risk', according to the industry standard [44]. Based on the derived PDFs, the probability of the system in different risk regions Pr(.) can be estimated as:

$$\Pr(\vartheta_{m\min} \le \hat{z}_b \le \vartheta_{m\max}) = \int_{\vartheta_{m\min}}^{\vartheta_{m\max}} p_{\hat{z}_b}(\hat{z}_b)d\hat{z}_b, \tag{31}$$

where $\vartheta_{m\min}$ and $\vartheta_{m\max}$ are the upper and lower bounds of m-th risk region, respectively.

According to Section II and III, the proposed PFS analysis method considering WEs of WFs can be summarized in Fig. 3.

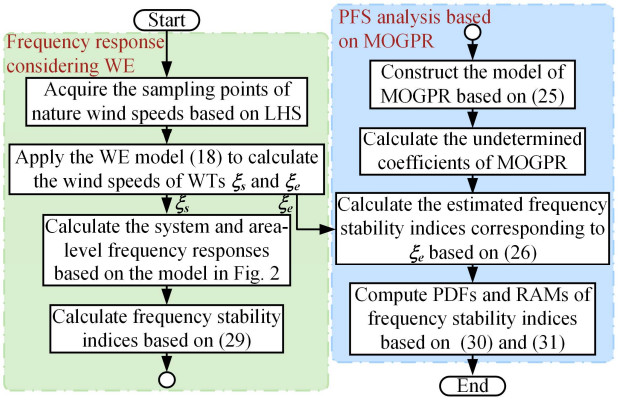

Fig. 3. Procedure of the proposed PFS analysis method considering WEs of WFs.

IV. Case Study

A. Case 1: IEEE 68-Bus Benchmark System

1) Example System

Case 1 is conducted in the IEEE 68-bus benchmark system [15] and implemented in MATLAB and Python as the simulation tools, where the power system dynamic models [39, 40], as presented in Fig. 2, are used. WTs are not equipped with additional frequency regulation control in Case 1 to show the obvious impact of WPG uncertainties on PFS. Three WFs are integrated into the system, as illustrated in Fig. 4. 20 WTs are in each WF. The layout of WTs is set as 4×5 with the interval of 200m at the height of 50m. The wind direction is consistent with the positive direction of the x-axis of the geographical coordinate system. The initial nature wind speeds of WFs are 8m/s. The nature wind speeds change at 0.1s randomly [14]. AGC starts after 30s [45]. The uncertainties of the changed nature wind speeds obey the following probabilistic distributions: The nature wind speed of WF1 follows *Weibull* (2.5, 4.5, 4); Those of WF2 and WF3 follow *Weibull* (2, 5, 3.5) with the correlation coefficient of 0.7. The rest of the parameters are presented in Appendix. It should be noted that the proposed WE model and PFS analysis method are generic and suitable for both short-term and long-term studies. In this paper, the widely-used Weibull function is selected for demonstration, which is usually used to quantify the uncertainty of the nature wind speed in long-term planning [15].

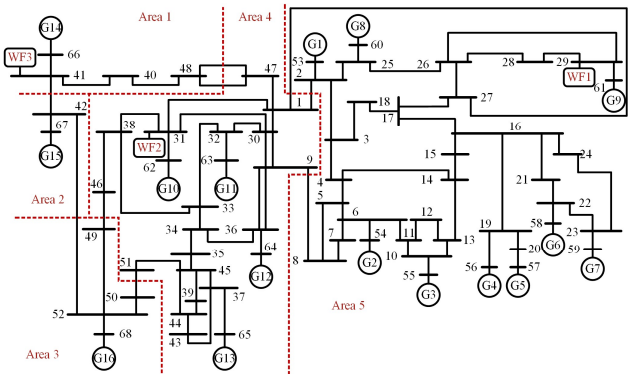

Fig. 4. IEEE 68-bus system integrated with three WFs.

2) Validation of Multiple Output Gaussian Process Regression for Probabilistic Frequency Stability Analysis Considering Wake Effects of Wind Farms

Firstly, the accuracy of the proposed WE model is verified by comparing it with the measurements, CFD, and Jensen and Gaussian analytical WE models presented in Fig. 5, where the measurements and results of CFD are from [46].

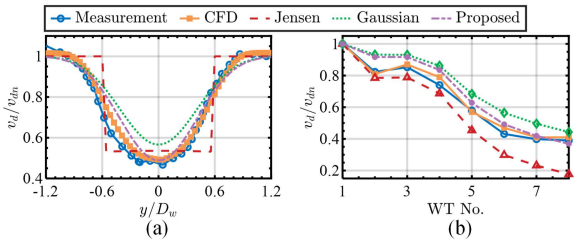

Fig. 5. Calculation results of WEs in the scenarios of [46]: (a) Single WT in Wieringermeer East; (b) WTs in Lillgrund WF.

From Fig. 5, compared with other analytical WE models, the results of the proposed model are closer to measurements, which demonstrates the accuracy of the proposed model. Although the results of the proposed model are less accurate than those of CFD, CFD is not suitable for PFS analysis since the simulation time of WEs by using CFD is much longer than that of power systems. Additionally, it can be seen in Fig. 5 (b) that the calculation errors of the proposed model associated with WTs located further along the wind direction are lower than those of WTs located closer. This observation does not mean that the proposed model has the higher accuracy for further WTs, which is just caused by the possible occurrence of positive and negative error offset. In detail, the situations where the calculated wind speed deficit by the proposed model is severer than the actual wind speed deficit are called positive errors in this paper. Also, the situations where the calculated wind speed deficit is milder than the actual wind speed deficit are called negative errors. These two types of errors exist simultaneously when the WE of one WT is calculated. For example, as shown in Fig. 5 (a), positive error at $y/D_w=1$ and negative error at $y/D_w=-0.4$. Moreover, the wind speed of the downstream WT is affected by the WEs of all upstream WTs. Thus, calculation errors are accumulated. When errors with the opposite nature happen to be accumulated, the overall error may be very small.

To verify the effectiveness of the proposed method, MCS considering the WEs of WFs (denoted as MCS-WE) is conducted 5000 times [13], the results of which are regarded as the baseline. Meanwhile, MCS ignoring the WEs of WFs (denoted as MCS-NWE) [13] is carried out to demonstrate the impact of the WEs on PFS. Moreover, the performance of the proposed method is compared with GPR. The Gaussian kernel is selected as the covariance kernel function, and the quantity of sampling data is chosen as 400 [35]. It should be noted that it is the first time to apply the GPR-based method in PFS. Thus, both GPR and MOGPR are novel methods in PFS analysis. The time of the frequency response simulation t_S, the WE calculation time t_W, the execution time of uncertainty propagation analysis methods t_M, and the total time t_T are illustrated in Table I.

TABLE I
TIME COST IN ANALYZING FN/FV AND ROCOF IN CASE 1

Time cost	t_S (s)	t_W (s)	t_M (s)	t_T (s)
MCS-NWE	191173.94	-	-	191173.94
MCS-WE	202927.13	257.28	-	203184.41
GPR	16233.77	20.70	26.63	16281.10
MOGPR	16234.42	20.54	8.32	16263.28

From Table I, t_W is significantly less than t_S, which means that the proposed WE model only brings a slight rise of the computational time in PFS analysis and thus is suitable for PFS analysis. Moreover, MCS-based methods are quite time-consuming. By comparison, t_S of GPR-based methods is greatly shorter than that of MCS-based methods. Furthermore, since MOGPR can calculate the FS indices of different areas simultaneously, t_M of MOGPR is shorter than that of GPR, which indicates the advantage of MOGPR in improving efficiency. Additionally, since the efficient scenario-based methods for analyzing the worst-case scenarios of power system FS considering WPG uncertainties and WEs are lacking, the worst-case scenarios need to be found from a large quantity of possible scenarios. Thus, the time cost of the worst scenario (WS) selection nearly equals that of MCS.

Moreover, the PDFs of FN/FV and RoCoF are shown in Fig. 6 to verify the accuracy of the proposed method, where WSs are also drawn. To save space, only the results of Area1, Area2, and the system are presented.

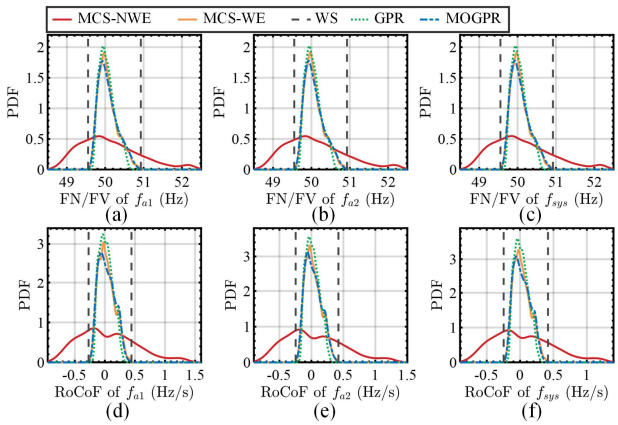

Fig. 6. PDF of FN/FV and RoCoF in Case 1: (a) FN/FV of Area 1; (b) FN/FV of Area 2; (c) FN/FV of the system; (d) RoCoF of Area 1; (e) RoCoF of Area 2; (f) RoCoF of the system.

As shown in Fig. 6, there are significant differences between the results from MCS-NWE and those from MCS-WE in both FN/FV and RoCoF, which indicates that ignoring the WEs of WFs in PFS analysis is inaccurate. The PDFs of FN/FV and RoCoF from MCS-NWE have fatter tails, which means FN/FV and RoCoF are more separated when ignoring the WEs of WFs, leading to a higher probability of frequency instability. To further illustrate the differences between considering and ignoring WEs, the wind speed of WF considering WEs and frequency responses when all nature wind speeds change to 7m/s are drawn in Fig. 7 as examples.

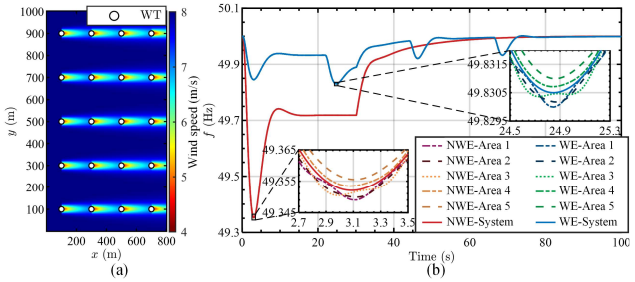

Fig. 7. (a) Wind speed of WFs considering WEs; (b) Frequency trajectories affected by the wind speed change.

From Fig. 7 (a), there are wind speed deficits at downstream WTs when considering WEs, which results in smaller power fluctuations under the same changes of the nature wind speed compared with those ignoring WEs. This contributes to a smaller frequency fluctuation, making the PDFs of FN/FV and RoCoF more concentrated. Moreover, from Fig. 7 (b), due to the time delay of WEs, the changing time points of wind speeds of WTs at different positions are different, which also leads to PDFs of RoCoF being more concentrated. Thus, the results demonstrate the necessity of considering the WEs of WFs in PFS analysis.

Moreover, to quantify the accuracy of different methods in calculating the PDFs of FN/FV and RoCoF presented in Fig. 6, the PDF shape difference s_* is introduced. It is defined as the Euclidean distance between the actual PDF $p_z(z)$ and the estimated PDF $p_{\hat{z}}(\hat{z})$, i.e., $\|p_z(z) - p_{\hat{z}}(\hat{z})\|$, as shown in Table II. The subscript of s_* is the FS index of the system and areas. For example, the FN/FV and RoCoF of frequency of Area a /system are denoted as F_{Aa} / F_{sys} and R_{Aa} / R_{sys}, respectively.

TABLE II
SHAPE DIFFERENCE OF PDFS OF FN/FV AND ROCOF IN CASE 1

Shape difference	$s_{F_{A1}}$	$s_{F_{A2}}$	$s_{F_{sys}}$	$s_{R_{A1}}$	$s_{R_{A2}}$	$s_{R_{sys}}$
GPR	2.02	2.01	2.01	4.08	4.18	4.18
MOGPR	1.01	1.02	1.02	2.14	1.72	2.23

From Table II, the PDFs from MOGPR have the higher similarity to the PDFs from MCS-WE in both FN/FV and RoCoF, compared with those from GPR. The results indicate the high accuracy merit of the proposed method in calculating the PDFs of FS indices. Moreover, from Fig. 6, although scenario-based WS selection gives the boundaries of FS indices, it cannot reflect the probability of WSs, which is also concerned in PFS, since preparing excessively for frequency violation scenarios with very low occurrence probabilities will greatly increase unnecessary reserve costs. By comparison, GPR and MOGPR use limited sampling points, i.e., scenarios, to build the corresponding models to analyze FS of power systems in all possible scenarios, thereby balancing efficiency and accuracy. In addition, the RAM can be formed based on the results in Fig. 6, as shown in Table III, where 'Green', 'Yellow', and 'Red' regions denote 'Low Risk', 'Medium Risk', and 'High Risk', respectively. Results presented in the row of 'MCS-WE' are the risk occurrence probability of frequency. Results shown in the row of rest methods are the absolute errors (AEs) between the risk occurrence probability from different methods and that from MCS-WE. To show the overall accuracy, the mean absolute errors (MAEs) are listed in the last column. The units of results in Table III are %.

TABLE III
RAM OF FN/FV AND ROCOF IN CASE 1

FN/FV (Hz)		<49.5	49.5~49.8	49.8~50.2	50.2~50.5	>50.5	MAE
Area 1	MCS-WE	0.00	11.05	62.23	19.38	7.33	-
	GPR	0.00	2.32	6.06	0.96	4.70	2.80
	MOGPR	0.00	0.83	2.12	0.66	0.63	0.85
Area 2	MCS-WE	0.00	11.02	62.27	19.37	7.34	-
	GPR	0.00	2.31	6.05	0.96	4.69	2.80
	MOGPR	0.00	0.83	2.12	0.67	0.62	0.84
System	MCS-WE	0.00	10.97	62.36	19.37	7.30	-
	GPR	0.00	2.21	6.14	0.90	4.68	2.80
	MOGPR	0.00	0.82	2.13	0.70	0.62	0.85
ROCOF (Hz/s)		<-0.5	-0.5~-0.4	-0.4~0.4	0.4~0.5	>0.5	MAE
Area 1	MCS-WE	0.00	0.00	99.70	0.30	0.00	-
	GPR	0.00	0.00	0.30	0.30	0.00	0.12
	MOGPR	0.00	0.00	0.13	0.13	0.00	0.05
Area 2	MCS-WE	0.00	0.00	99.86	0.14	0.00	-
	GPR	0.00	0.00	0.14	0.14	0.00	0.06
	MOGPR	0.00	0.00	0.04	0.04	0.00	0.02
System	MCS-WE	0.00	0.00	99.89	0.11	0.00	-
	GPR	0.00	0.00	0.11	0.11	0.00	0.04
	MOGPR	0.00	0.00	0.04	0.04	0.00	0.01

In Table III, the risk occurrence probability of FN/FV is mainly located in the low and medium-risk regions. The occurrence probability of high-risk regions is relatively low. The maximal AE of RAM of FN/FV from GPR is 6.14%. By comparison, that from MOGPR is 2.13%. Moreover, the maximal MAE of RAM of FN/FV from GPR is 2.80%, and that from MOGPR is 0.85%. The results indicate that the accuracy of MOGPR in analyzing the RAM of FN/FV is better than that of GPR. For RAM of RoCoF, the risk occurrence probability is mainly located in the low-risk region, rarely in the medium-risk regions. The maximal AE from GPR is 0.30%, and that from MOGPR is 0.13%. The maximal MAE from GPR is 0.12%, and that from MOGPR is 0.05%. Thus, the results demonstrate the high accuracy merit of the proposed method in analyzing the RAMs of FS indices compared with GPR.

3) **Impact of Different Factors on Probabilistic Frequency Stability**

a) Wind Direction

The angle between the wind direction and the positive direction of the x-axis is set as 30°, 45°, and 90°, respectively, to investigate the impact of wind direction on PFS. Firstly, the accuracy of different methods in calculating PDFs of FN/FV and RoCoF and analyzing the RAM are shown in Table IV.

TABLE IV
PERFORMANCE IN ANALYZING FN/FV AND ROCOF AFFECTED BY WIND DIRECTIONS

Shape difference		$s_{F_{A1}}$	$s_{F_{A2}}$	$s_{F_{sys}}$	$s_{R_{A1}}$	$s_{R_{A2}}$	$s_{R_{sys}}$
θ_{xy}=30°	GPR	2.58	2.58	2.57	8.18	7.91	8.22
	MOGPR	1.98	1.98	1.98	4.25	4.62	4.67
θ_{xy}=45°	GPR	2.85	2.83	2.81	5.47	5.47	5.67
	MOGPR	1.68	1.71	1.65	2.14	2.02	2.29
θ_{xy}=90°	GPR	2.33	2.32	2.32	4.76	4.94	4.82
	MOGPR	1.18	1.19	1.19	2.33	1.87	2.45
MAE		$e_{F_{A1}}$	$e_{F_{A2}}$	$e_{F_{sys}}$	$e_{R_{A1}}$	$e_{R_{A2}}$	$e_{R_{sys}}$
θ_{xy}=30°	GPR	2.17	2.17	2.17	0.00	0.00	0.00
	MOGPR	1.01	1.01	1.02	0.00	0.00	0.00
θ_{xy}=45°	GPR	3.03	3.02	3.01	0.00	0.00	0.00
	MOGPR	0.45	0.38	0.44	0.00	0.00	0.00
θ_{xy}=90°	GPR	1.89	1.89	2.88	0.00	0.00	0.00
	MOGPR	0.63	0.63	0.63	0.00	0.00	0.00

As shown in Table IV, the maximal PDF shape difference of FN/FV and RoCoF from GPR is 8.22. In comparison, that from MOGPR is 4.67. For the RAM results, the maximal MAE of FN/FV from GPR is 3.03%, and that from MOGPR is 1.02%. The maximal MAE of RoCoF from both GPR and MOGPR is 0.00% since the risk occurrence probability of the low-risk region is 100.00%. The results verify the accuracy of the proposed method in PFS analysis.

Moreover, the wind speed of WFs at the height of 50m and RAM results are presented in Fig. 8 and Fig. 9 to show the impact of wind direction on PFS. Since the risk probability of RoCoF in the low-risk region is 100.00%, only the RAMs of FN/FV are drawn in Fig. 9 to save space.

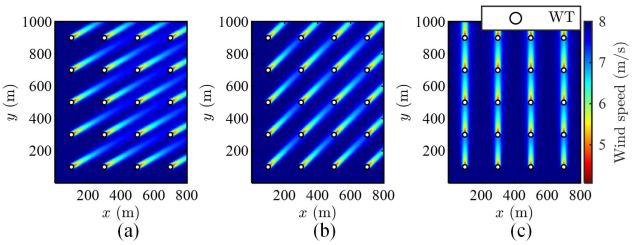

Fig. 8. WEs of WFs at different wind directions: (a) θ_{xy}=30°; (b) θ_{xy}=45°; (c) θ_{xy}=90°.

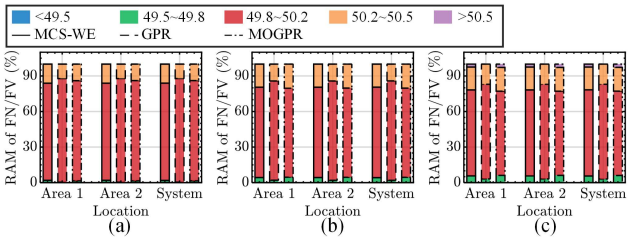

Fig. 9. RAM of FN/FV at different wind directions: (a) θ_{xy}=30°; (b) θ_{xy}=45°; (c) θ_{xy}=90°.

From Fig. 8 and Fig. 9, the change of wind direction leads to the distance change of WTs in the wind direction. Taking the WT at the position (100m, 100m, 50m) as an example, the nearest WTs directly below in the wind direction are the WT at (500m, 300m, 50m) (approximately below when θ_{xy}=30°), the WT at (300m, 300m, 50m) (when θ_{xy}=45°), and the WT at (300m, 300m, 50m) (when θ_{xy}=90°), respectively. The streamwise distances are 446.41m, 282.84m, and 200m, separately. The wind speed deficit will increase with the rise of wind direction due to the rise of the WE strength. Under the same change of the nature wind speed, before AGC starts, the quantity of WTs experiencing power fluctuations is the most when θ_{xy}=90°, and that is the least when θ_{xy}=30°. Thus, the risk occurrence probability of FN/FV is mainly in the low-risk region when θ_{xy}=30°. When θ_{xy}=45°, the probability in the low-risk region reduces, and the probability in medium-risk regions rises. When θ_{xy}=90°, the risk occurrence probability of FN/FV is more separated, and there is the probability of frequency being in the high-risk region.

b) Terrain

The ridge, the circular hill, and the rolling terrain are involved in the case studies to study the impact of different terrains on PFS. The terrain parameters of the height and the length are set as 50m and 150m. The accuracy of different methods, the wind speed of WFs, and the RAM results are illustrated in Table V, Fig. 10, and Fig. 11, separately.

TABLE V
PERFORMANCE IN ANALYZING FN/FV AND ROCOF AFFECTED BY TERRAINS

Shape difference		$s_{F_{A1}}$	$s_{F_{A2}}$	$s_{F_{sys}}$	$s_{R_{A1}}$	$s_{R_{A2}}$	$s_{R_{sys}}$
Ridge	GPR	2.99	2.99	2.99	5.22	5.36	5.46
	MOGPR	1.42	1.42	1.42	2.40	2.60	2.63
Circular hill	GPR	2.19	2.19	2.19	4.27	4.38	4.64
	MOGPR	0.70	0.71	0.71	1.70	1.65	1.77
Rolling terrain	GPR	2.29	2.29	2.29	4.65	4.70	4.88
	MOGPR	0.95	0.96	0.96	1.15	1.21	1.26
MAE		$e_{F_{A1}}$	$e_{F_{A2}}$	$e_{F_{sys}}$	$e_{R_{A1}}$	$e_{R_{A2}}$	$e_{R_{sys}}$
Ridge	GPR	4.19	4.18	4.17	0.79	0.36	0.32
	MOGPR	0.53	0.53	0.52	0.06	0.11	0.11
Circular hill	GPR	2.33	2.32	2.31	0.02	0.00	0.00
	MOGPR	1.08	1.08	1.08	0.01	0.00	0.00
Rolling terrain	GPR	2.79	2.78	2.77	0.00	0.00	0.00
	MOGPR	1.11	1.11	1.11	0.00	0.00	0.00

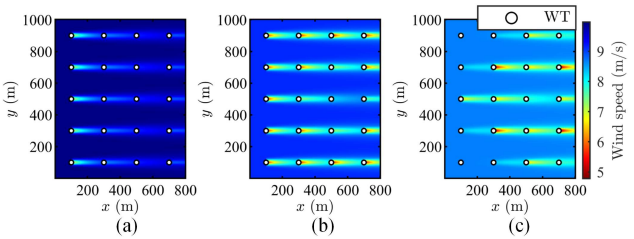

Fig. 10. WEs of WFs at different terrains: (a) Ridge; (b) Circular hill; (c) Rolling terrain.

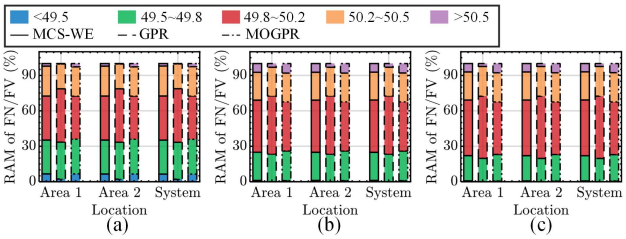

Fig. 11. RAM of FN/FV at different terrains: (a) Ridge; (b) Circular hill; (c) Rolling terrain.

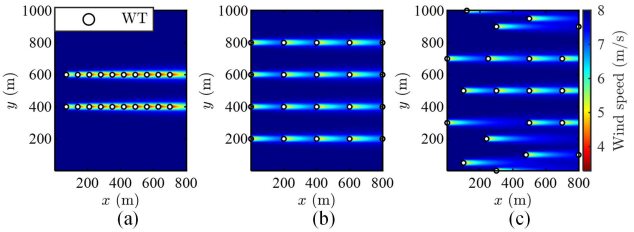

Fig. 12. WEs of WFs with different layouts: (a) 2×10 ; (b) 5×4 ; (c) Optimized layout.

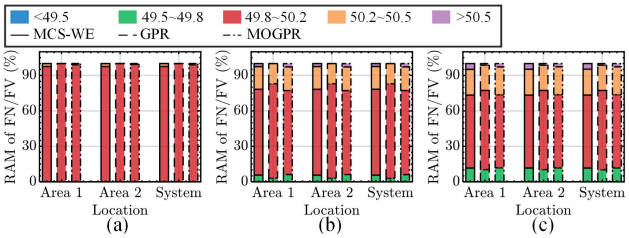

Fig. 13. RAM of FN/FV with different layouts: (a) 2×10 ; (b) 5×4 ; (c) Optimized layout.

According to Table V, the PDF shape differences and the MAEs of RAM from MOGPR are lower than those from GPR, which indicates that the accuracy of MOGPR is higher than that of GPR. From Fig. 10 and Fig. 11, after considering different terrains, the level of the nature wind speed and the WE strength are affected. In case studies, the wind speed deficit at the ridge is the smallest. The level of nature wind speed at the ridge is the highest, and those at the circular hill and the rolling terrain are relatively low, which can be regarded as the difference of wind power penetration. Thus, when the wind speed changes, the power fluctuations of WTs are most obvious at the ridge. As a result, the risk occurrence probability of FN/FV is separated in different risk regions at the ridge. At the circular hill and the rolling terrain, the probability in high-risk and medium-risk regions reduces, and the probability in the low-risk region rises.

c) Wind Turbine Layout

The position of WTs in every WF is changed to 2×10 , 5×4 , and the optimized layout with the objective of minimizing the unit generation cost [47], respectively, to demonstrate the impact of layout on PFS. The accuracy of different methods, the wind speed of WFs, and the RAM results are presented in Table VI, Fig. 12, and Fig. 13, separately.

TABLE VI
PERFORMANCE IN ANALYZING FN/FV AND ROCOF AFFECTED BY WIND TURBINE LAYOUTS

Shape difference		$s_{F_{A1}}$	$s_{F_{A2}}$	$s_{F_{sys}}$	$s_{R_{A1}}$	$s_{R_{A2}}$	$s_{R_{sys}}$
2×10	GPR	3.98	3.97	3.97	7.06	6.93	6.79
	MOGPR	1.99	2.00	2.00	3.08	3.15	3.21
5×4	GPR	2.33	2.32	2.32	4.76	4.94	4.82
	MOGPR	1.18	1.19	1.19	2.33	1.87	2.45
Optimized layout	GPR	2.26	2.26	2.24	5.95	6.06	6.52
	MOGPR	1.64	1.66	1.65	2.52	2.66	2.68
MAE		$e_{F_{A1}}$	$e_{F_{A2}}$	$e_{F_{sys}}$	$e_{R_{A1}}$	$e_{R_{A2}}$	$e_{R_{sys}}$
2×10	GPR	0.97	0.97	0.97	0.00	0.00	0.00
	MOGPR	0.59	0.68	0.59	0.00	0.00	0.00
5×4	GPR	2.89	2.89	2.88	0.00	0.00	0.00
	MOGPR	0.63	0.63	0.63	0.00	0.00	0.00
Optimized layout	GPR	2.14	2.14	2.12	0.00	0.00	0.00
	MOGPR	0.81	0.83	0.81	0.00	0.00	0.00

Results in Table VI show that both the PDF shape differences and the MAEs of RAM from MOGPR are lower than those from GPR. Based on Fig. 12 and Fig. 13, different layouts change the relative position of WTs, thereby changing the strength of the WEs in WFs, which results in more wind speed deficits, as illustrated in Fig. 12, and less conspicuous power fluctuations of WTs with a narrower layout. Thus, the risk occurrence probability of FN/FV is almost all in the low-risk region with 2×10 layout due to the high WE strength. When the layout is separated, since the WE strength is low, the probability in the low-risk region reduces, that in medium-risk regions increases, and even that in high-risk regions occurs.

It should be noted that though the wind direction, the terrain, and the WT layout are independent factors with different properties, i.e., the meteorological factor, the geographical factor, and the factor determined by different system planning purposes, respectively, their impacts on WEs and PFS are not independent. The reason is that the relative distance between WTs directly affects WEs and then PFS. Any one of these three factors can affect the relative distance, as characterized in Section II.A. Thus, though the change of one factor will not contribute to the change of another factor, it will affect the impact of another factor on WEs and PFS. Since their impacts on WEs and PFS are interwoven with each other, the impact analysis of individual factors is beneficial for revealing the general patterns of their impacts.

B. Case 2: Large-Scale Realistic Power System in East China

1) **Example System**

Case 2 is conducted in a large-scale power system modified based on the realistic two-area system in East China, including 1958 buses and 56 generators, to demonstrate the scalability of the proposed method. Five WFs are integrated into the system, as presented in Fig. 14, where WF1, WF2, and WF5 are onshore. WF3 and WF4 are offshore. The nature wind speeds of WF1 and

WF2 follow *Weibull* (2.5, 4.5, 4) with the correlation coefficient of 0.7. Those of WF3, WF4, and WF5 follow *Weibull* (2, 5, 3.5), *Weibull* (1.5, 2, 4), and *Weibull* (1.5, 3.5, 5), respectively. The rest settings of WFs, MCS, GPR, and MOGPR are the same as those in Case 1.

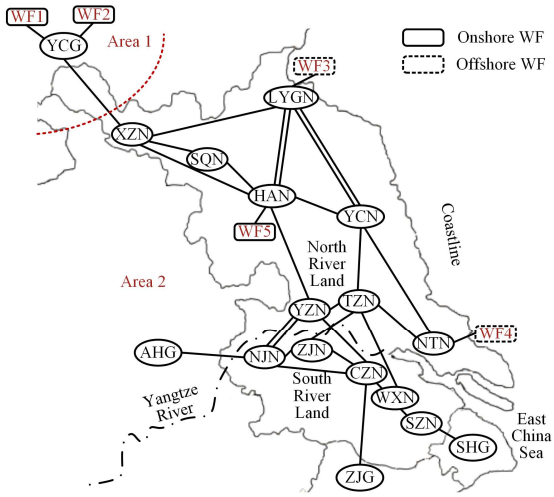

Fig. 14. Large-scale power system integrated with five WFs.

2) **Scenario 1: Probabilistic Frequency Stability Analysis Considering Wake Effects of Wind Farms Without Additional Frequency Regulation Control**

Firstly, the case study is carried out under the scenario that WFs are not equipped with additional frequency regulation control. The time costs of different methods in analyzing PFS are listed in Table VII.

TABLE VII
TIME COST IN ANALYZING FN/FV AND ROCOF IN SCENARIO 1 CASE 2

Time cost	t_S (s)	t_W (s)	t_M (s)	t_T (s)
MCS	692876.29	430.71	-	693307.00
GPR	55428.08	34.55	13.35	55475.98
MOGPR	55428.73	34.64	3.89	55467.26

From Table VII, similar observations as those in Case 1 can be obtained, i.e., the total time costs of GPR and MOGPR are significantly lower than that of MCS, and the execution time of MOGPR is shorter than that of GPR due to the multi-output structure. In addition, since the system in Case 1 has 5 areas, whereas that in Case 2 has 2 areas, the quantity of analyzed FS indices in Case 2 is fewer than that in Case 1. Thus, the execution time of GPR and MOGPR in Case 2 is shorter than that in Case 1.

The PDFs of FS indices calculated based on different methods are presented in Fig. 15, where WSs are also drawn. The shape differences of PDFs are computed to assess the accuracy of different methods in calculating PDFs, as illustrated in Table VIII. RAM derived from the results shown in Fig. 15 is listed in Table IX. Since the probability of RoCoF in the low-risk region is 100%, and all methods obtain the same results, only the RAM results of FN/FV are presented to save space.

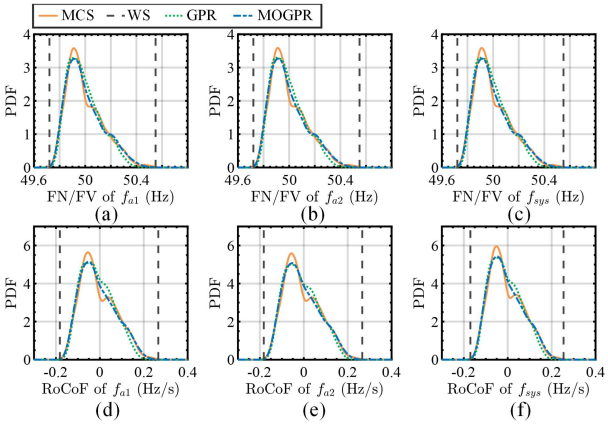

Fig. 15. PDF of FN/FV and RoCoF in Scenario 1 Case 2: (a) FN/FV of Area 1; (b) FN/FV of Area 2; (c) FN/FV of the system; (d) RoCoF of Area 1; (e) RoCoF of Area 2; (f) RoCoF of the system.

TABLE VIII
SHAPE DIFFERENCE OF PDFS OF FN/FV AND ROCOF IN SCENARIO 1 CASE 2

Shape difference	$s_{F_{A1}}$	$s_{F_{A2}}$	$s_{F_{sys}}$	$s_{R_{A1}}$	$s_{R_{A2}}$	$s_{R_{sys}}$
GPR	2.38	2.39	2.39	4.04	3.31	3.58
MOGPR	1.58	1.59	1.59	2.52	2.52	2.59

TABLE IX
RAM OF FN/FV IN SCENARIO 1 CASE 2

FN/FV (Hz)		<49.5	49.5~49.8	49.8~50.2	50.2~50.5	>50.5	MAE
Area 1	MCS	0.00	3.27	85.72	10.79	0.22	-
	GPR	0.00	1.04	3.84	2.61	0.19	1.53
	MOGPR	0.00	0.15	0.46	0.77	0.15	0.30
Area 2	MCS	0.00	3.22	85.85	10.72	0.21	-
	GPR	0.00	1.03	3.83	2.62	0.19	1.54
	MOGPR	0.00	0.15	0.45	0.75	0.15	0.31
System	MCS	0.00	3.22	85.81	10.75	0.22	-
	GPR	0.00	1.04	3.84	2.61	0.19	1.53
	MOGPR	0.00	0.15	0.46	0.76	0.15	0.30

By comparing the results in Table VIII with those in Table II, though the system in Case 2 is much larger than those in Case 1 and with more uncertainties, the accuracy of the proposed method in calculating the PDFs of FS indices in Case 2 is close to that in Case 1. Moreover, the RAM results in Case 2, as illustrated in Table IX, also demonstrate the high accuracy of MOGPR, with 0.31% maximal MAE. These results indicate the scalability of MOGPR in analyzing large-scale power systems with more uncertainties considering both onshore and offshore WFs and WEs.

3) **Scenario 2: Probabilistic Frequency Stability Analysis Considering Wake Effects of Wind Farms with**

Additional Frequency Regulation Control

It can be seen in Table IX that FN/FV has the probability to be in the medium-risk and even high-risk regions when there is no frequency regulation control in WFs. Thus, to improve the PFS of the system, additional frequency regulation control is equipped in Scenario 2. Different methods are adopted to analyze PFS in this scenario. The comparison of time costs, PDFs of FN/FV, shape differences of FN/FV PDFs, and the RAM of FN/FV among different methods are presented in Table X, Fig. 16, Table XI, and Table XII, separately.

TABLE X
TIME COST IN ANALYZING FN/FV AND ROCOF IN SCENARIO 2 CASE 2

Time cost	t_S (s)	t_W (s)	t_M (s)	t_T (s)
MCS	692897.42	431.03	-	693328.45
GPR	55430.76	34.62	13.30	55478.68
MOGPR	55431.28	34.59	3.91	55469.78

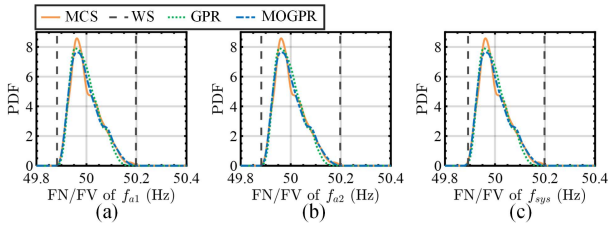

Fig. 16. PDF of FN/FV in Scenario 2 Case 2: (a) Area 1; (b) Area 2; (c) System.

TABLE XI
SHAPE DIFFERENCE OF FN/FV PDFS IN SCENARIO 2 CASE 2

Shape difference	$s_{F_{A1}}$	$s_{F_{A2}}$	$s_{F_{sys}}$
GPR	3.67	3.69	3.69
MOGPR	2.55	2.56	2.56

TABLE XII
RAM OF FN/FV IN SCENARIO 2 CASE 2

FN/FV (Hz)		<49.5	49.5~49.8	49.8~50.2	50.2~50.5	>50.5	MAE
Area 1/	MCS	0.00	0.00	100.00	0.00	0.00	-
Area 2/	GPR	0.00	0.00	0.00	0.00	0.00	0.00
System	MOGPR	0.00	0.00	0.00	0.00	0.00	0.00

According to the results, the time costs and errors of MOGPR are close to those in Scenario 1, which demonstrates that MOGPR is applicable for PFS analysis of power systems integrated with WFs with additional frequency regulation control. Moreover, by comparing Table IX with Table XII, after applying additional frequency regulation control, the probability of FN/FV in the medium-risk and high-risk regions is greatly reduced to 0%, and FN/FV only exists in the low-risk region. The results illustrate that applying additional frequency regulation control in WFs can effectively enhance the PFS of power systems affected by WPG uncertainties.

V. CONCLUSION

In this paper, a method for PFS analysis considering the WEs of WFs is proposed. A WE model considering multiple factors, i.e., the terrain, the wind direction, and the time delay of wind flow, is proposed. Moreover, the impact of different factors on PFS is investigated. The analysis results reveal that:

1) Compared with the numerical uncertainty propagation analysis methods, the proposed method greatly improves the efficiency of PFS analysis. Compared with GPR, MOGPR can simultaneously analyze the probabilistic stability of the system frequency and the area-level frequency and consider the relationship between them with higher efficiency and accuracy. Compared with other approximation approaches, including PCE and LRA, both MOGPR and GPR only require sampling data, which are more suitable for analyzing uncertainties with complicated correlations, including the WEs of WFs.
2) Compared with conventional analytical WE models, the proposed WE model considers multiple factors, which can reflect the WEs of WFs more realistically and can be easily integrated into PFS analysis. Moreover, the time cost of the proposed model is greatly shorter than that of the frequency response simulation, which is suitable for PFS analysis.
3) The impacts of multiple factors related to WEs on PFS are studied. The results of case studies reveal that the change of the wind direction, the terrain, and the layout will contribute to the change of the WE strength. Specifically, a lower wind speed deficit and a higher level of the nature wind speed will lead to higher WPG penetrations, more obvious power fluctuations of WTs, more distributed PDFs of FS indices, and the probability increase of frequency in high and medium-risk regions of instability.
4) The necessity and significance of considering the WEs of WFs in PFS analysis are revealed based on case studies. The ignorance of the WEs of WFs in PFS analysis will result in a higher probability of frequency instability, which is inaccurate and leads to a conservative frequency regulation strategy and increased frequency reserve costs. To mitigate the degradation of PFS caused by WPG uncertainties considering WEs, the additional frequency regulation control for WTs can be adopted based on PFS analysis results.

Additionally, when the sampling data are disturbed by noises or only limited data can be acquired, the accuracy of the proposed method will be inevitably affected. Thus, the robustness improvement of the proposed method needs to be studied. In addition, since the proposed method is generic, it can be extended to probabilistic stability analysis associated with other stability issues and other uncertainty types. These research topics will be our future studies.

APPENDIX

Parameters of WEs: C_T=0.42 , k_w=0.042 , h_d=50 m , $D_w = 40$ m , $\gamma = 0.143$. WT parameters (p.u.): $C_p = 10$, $X_{pf} = 0.02$, $X_{pd} = 0.2$, $X_{pq} = 0.2$, $I_{psdref} = 0$, $V_{dcref} = 1$. Parameters of frequency regulation (p.u.): $R. = 0.05$, $\beta = 0.416$, $T_{ij} = 0.2$, $K_{Pa} = 1$, $K_{Ia} = 0.5$.

ACKNOWLEDGMENT

The authors would like to thank the support from the State Grid Jiangsu Electric Power Company in China.

REFERENCES

[1] K. S. Ratnam, K. Palanisamy, and G. Yang, "Future low-inertia power systems: Requirements, issues, and solutions - a review," *Renew. Sustain. Energy Rev.*, vol. 124, May 2020, Art. no 109773.

[2] G. Magdy, G. Shabib, A. A. Elbaset, and Y. Mitani, "Optimized coordinated control of LFC and SMES to enhance frequency stability of a real multi-source power system considering high renewable energy penetration," *Protection Control Modern Power Syst.*, vol. 3, no. 4, pp. 1-15, Oct. 2018.

[3] J. Wen, S. Bu, and F. Li, "Two-level ensemble methods for efficient assessment and region visualization of maximal frequency deviation risk," *IEEE Trans. Power Syst.*, vol. 38, no. 1, pp. 643-655, Jan. 2023.

[4] K. N. Hasan, R. Preece, and J. V. Milanović, "Existing approaches and trends in uncertainty modelling and probabilistic stability analysis of power systems with renewable generation," *Renew. Sustain. Energy Rev.*, vol. 101, pp. 168-180, Mar. 2019.

[5] A. P. Gupta, A. Mitra, A. Mohapatra, and S. N. Singh, "A multi-machine equivalent model of a wind farm considering LVRT characteristic and wake effect," *IEEE Trans. Sustain. Energy*, vol. 13, no. 3, pp. 1396-1407, Jul. 2022.

[6] C. Guo, F. Gan, D. Du, Y. Guo, and H. Cheng, "Applicability evaluation of wind farm impedance models using different aggregation methods for high frequency oscillation analysis," *IEEE Trans. Power Deliv.*, vol. 29, no. 4, pp. 2231-2241, Aug. 2024.

[7] L. M. Fernández, C. A. García, J. R. Saenz, and F. Jurado, "Equivalent models of wind farms by using aggregated wind turbines and equivalent winds," *Energy Convers. Manag.*, vol. 50, no. 3, pp. 691-704, Mar. 2009.

[8] A. Marinopoulos et al., "Investigating the impact of wake effect on wind farm aggregation," in *2011 IEEE Trondheim PowerTech*, Trondheim, Norway, 2011, pp. 1-5.

[9] M. H. Johnson and D. C. Aliprantis, "Analysis of series-DC offshore wind plants with aerodynamic wake effects," *IEEE Trans. Sustain. Energy*, vol. 8, no. 4, pp. 1706-1714, Oct. 2017.

[10] L. Xiong et al., "Optimal allocation of energy storage system in DFIG wind farms for frequency support considering wake effect," *IEEE Trans. Power Syst.*, vol. 37, no. 3, pp. 2097-2112, May 2022.

[11] M. Ali, I. S. Ilie, J. V. Milanovic, and G. Chicco, "Wind farm model aggregation using probabilistic clustering," *IEEE Trans. Power Syst.*, vol. 28, no. 1, pp. 309-316, Feb. 2013.

[12] X. Han, Y. Qu, P. Wang, and J. Yang, "Four-dimensional wind speed model for adequacy assessment of power systems with wind farms," *IEEE Trans. Power Syst.*, vol. 28, no. 3, pp. 2978-2985, Aug. 2013.

[13] S. Bu, J. Wen, and F. Li, "A generic framework for analytical probabilistic assessment of frequency stability in modern power system operational planning," *IEEE Trans. Power Syst.*, vol. 34, no. 5, pp. 3973-3976, Sep. 2019.

[14] J. Wen, S. Bu, and H. Xin, "Probabilistic assessment on area-level frequency nadir/vertex for operational planning," *IEEE Open Access J. Power Energy*, vol. 8, pp. 341-351, Aug. 2021.

[15] J. Wen, S. Bu, F. Li, and P. Du, "Risk assessment and mitigation on area-level RoCoF for operational planning," *Energy*, vol. 228, Aug. 2021, Art. no 120632.

[16] M. M. Amiri, M. Shadman, and S. F. Estefen, "A review of physical and numerical modeling techniques for horizontal-axis wind turbine wakes," *Renew. Sustain. Energy Rev.*, vol. 193, Apr. 2024, Art. no 114279.

[17] Y. Zhang et al., "A review on numerical development of tidal stream turbine performance and wake prediction," *IEEE Access*, vol. 8, pp. 79325-79337, Apr. 2020.

[18] L. Zhang, X. Zhang, and Q. Wang, "A review of wind farm wake characteristics under complex terrain conditions," in *2023 7th Int. Conf. Smart Grid Smart Cities*, Lanzhou, China, 2023, pp. 534-539.

[19] Y. Dong et al., "Review on research about wake effects of offshore wind turbines," *Energy Eng.*, vol. 119, no. 4, pp. 1341-1360, 2022.

[20] R. Shakoor, M. Y. Hassan, A. Raheem, and Y.-K. Wu, "Wake effect modeling: A review of wind farm layout optimization using Jensen's model," *Renew. Sustain. Energy Rev.*, vol. 58, pp. 1048-1059, May 2016.

[21] B. López, A. Guggeri, M. Draper, and G. Usera, "Assessment of a heterogeneous computing CFD code in wind farm simulations," *J. Phys. Conf. Ser.*, vol. 2265, no. 4, 2022, Art. no 042046.

[22] X. Lyu, Y. Jia, and Z. Xu, "A novel control strategy for wind farm active power regulation considering wake interaction," *IEEE Trans. Sustain. Energy*, vol. 11, no. 2, pp. 618-628, Apr. 2020.

[23] S. Frandsen et al., "Analytical modelling of wind speed deficit in large offshore wind farms," *Wind Energy*, vol. 9, pp. 39-53, Jan. 2006.

[24] M. Bastankhah and F. Porté-Agel, "A new analytical model for wind-turbine wakes," *Renew. Energy*, vol. 70, pp. 116-123, Oct. 2014.

[25] W. Xiang, P. Zhou, L. Ban, M. Zhang, Z. Xiang, and R. Huang, "Equivalent modeling of wind farms considering wake effects and analysis of probability of sub-synchronous oscillations," in *2021 Int. Conf. Power Syst. Technol.*, Haikou, China, 2021, pp. 91-98.

[26] Z. Xinyan and W. Weiqing, "Wind farm and wake effect modeling for simulation of a studied power system," in *2009 IEEE/PES Power Syst. Conf. Expo.*, Seattle, WA, USA, 2009, pp. 1-6.

[27] P. Wang, Z. Zhang, Q. Huang, N. Wang, X. Zhang, and W. J. Lee, "Improved wind farm aggregated modeling method for large-scale power system stability studies," *IEEE Trans. Power Syst.*, vol. 33, no. 6, pp. 6332-6342, Nov. 2018.

[28] K. Ye, J. Zhao, H. Zhang, and Y. Zhang, "Data-driven probabilistic voltage risk assessment of MiniWECC system with uncertain PVs and wind generations using realistic data," *IEEE Trans. Power Syst.*, vol. 37, no. 5, pp. 4121-4124, Sep. 2022.

[29] S. Xia, X. Luo, K. W. Chan, M. Zhou, and G. Li, "Probabilistic transient stability constrained optimal power flow for power systems with multiple correlated uncertain wind generations," *IEEE Trans. Sustain. Energy*, vol. 7, no. 3, pp. 1133-1144, Jul. 2016.

[30] Y. Gao et al., "Analytical probabilistic power flow and global sensitivity analysis of distribution systems based on Gaussian mixture model of input-output variables," *IEEE Trans. Power Syst.*, vol. 39, pp. 5283-5296, May 2024.

[31] Z. Wang and S. Bu, "Probabilistic frequency stability analysis considering dynamics of wind power generation with different control strategies," *IEEE Trans. Power Syst.*, vol. 39, no. 5, pp. 6412-6425, Sep. 2024.

[32] K. Ye, J. Zhao, N. Duan, and D. A. Maldonado, "Stochastic power system dynamic simulation and stability assessment considering dynamics from correlated loads and PVs," *IEEE Trans. Ind. Appl.*, vol. 58, no. 6, pp. 7764-7775, Nov./Dec. 2022.

[33] W. Chen, X. Xie, D. Wang, H. Liu, and H. Liu, "Probabilistic stability analysis of subsynchronous resonance for series-compensated DFIG-based wind farms," *IEEE Trans. Sustain. Energy*, vol. 9, no. 1, pp. 400-409, Jan. 2018.

[34] Y. Jiang, T. H. Ortmeyer, M. Fan, and X. Ai, "Data-driven low-rank tensor approximation for fast grid integration of commercial EV charging stations considering demand uncertainties," *IEEE Trans. Smart Grid*, vol. 14, no. 1, pp. 517-529, Jan. 2023.

[35] K. Ye, J. Zhao, N. Duan, and Y. Zhang, "Physics-informed sparse Gaussian process for probabilistic stability analysis of large-scale power system with dynamic PVs and loads," *IEEE Trans. Power Syst.*, vol. 38, no. 3, pp. 2868-2879, May 2023.

[36] H. Liu, Y. S. Ong, X. Shen, and J. Cai, "When Gaussian process meets big data: A review of scalable GPs," *IEEE Trans. Neural Netw. Learn. Syst.*, vol. 31, no. 11, pp. 4405-4423, Nov. 2020.

[37] W. Weng, P. A. Taylor, and J. L. Walmsley, "Guidelines for airflow over complex terrain: Model developments," *J. Wind Eng. Ind. Aerodyn.*, vol. 86, no. 2, pp. 169-186, Jun. 2000.

[38] Q. Chen, S. Bu, and C. Y. Chung, "Small-signal stability criteria in power electronics-dominated power systems: A comparative review," *J. Modern Power Syst. Clean Energy*, vol. 12, no. 4, pp. 1003-1018, Jul. 2024.

[39] W. Du, H. Wang, and S. Bu, "Linearized model of a power system with a grid-connected variable speed wind generator," in *Small-signal stability analysis of power systems integrated with variable speed wind generators*, Cham, Switzerland: Springer, 2018, pp. 27-40.

[40] P. Kundur, "Control of active power and reactive power," in *Power system stability and control*, New York, NY, USA: McGraw-Hill, 1994, pp. 581-626.
[41] M. A. Alvarez, L. Rosasco, and N. D. Lawrence, "Kernels for vector-valued functions: A review," *Found. Trends Mach. Learn.*, vol. 4, no. 3, pp. 195-266, Jun. 2012.
[42] P. Kundur et al., "Definition and classification of power system stability IEEE/CIGRE joint task force on stability terms and definitions," *IEEE Trans. Power Syst.*, vol. 19, no. 3, pp. 1387-1401, May 2004.
[43] L. Xiong, X. Liu, Y. Liu, and F. Zhuo, "Modeling and stability issues of voltage-source converter-dominated power systems: A review," *CSEE J. Power Energy Syst.*, vol. 8, no. 6, pp. 1530-1549, Nov. 2022.
[44] National Electricity Transmission System (NETS), *Security and quality of supply standard (SQSS)*, Oct. 19, 2024. [Online]. Available: https://www.nationalgrideso.com/industry-information/codes/security-and-quality-supply-standard-sqss
[45] J. H. Eto et al., "Use of frequency response metrics to assess the planning and operating requirements for reliable integration of variable renewable generation," Lawrence Berkeley National Laboratory, USA, Rep. LBNL-4142E, 2010.
[46] DTU Wind, Technical University of Denmark, *Pywake 2.5.0: An open-source wind farm simulation tool*, Oct. 19, 2024. [Online]. Available: https://gitlab.windenergy.dtu.dk/TOPFARM/PyWake
[47] G. Mosetti, C. Poloni, and B. Diviacco, "Optimization of wind turbine positioning in large windfarms by means of a genetic algorithm," *J. Wind Eng. Ind. Aerodyn.*, vol. 51, no. 1, pp. 105-116, Jan. 1994.

Zhaoyuan Wang (S'24) received the B.S. degree in electrical engineering and its automation from North China Electric Power University, Baoding, China, in 2018 and the M.S. degree in electrical engineering from Huazhong University of Science and Technology, Wuhan, China, in 2021. He is currently pursuing the Ph.D. degree with the Department of Electrical and Electronic Engineering, The Hong Kong Polytechnic University, Hong Kong SAR, China. His current research interests include uncertainty quantification of renewable penetrated power systems and stability analysis of cyber-physical power systems.

Siqi Bu (S'11-M'12-SM'17) received the Ph.D. degree from the electric power and energy research cluster, The Queen's University of Belfast, Belfast, U.K., where he continued his postdoctoral research work before entering industry. Then he was with National Grid UK as an experienced UK National Transmission System Planner and Operator. He is an Associate Professor and Associate Head with Department of Electrical and Electronic Engineering, The Hong Kong Polytechnic University, Kowloon, Hong Kong, and Associate Director of Research Centre for Grid Modernisation. He is also a Chartered Engineer with UK Royal Engineering Council, London, U.K. and a Fellow of IET. His research interests include power system stability, operation and economics considering renewable energy integration, smart grid application and transport electrification.

Dr Bu is an Editor of IEEE Transactions on Power Systems, IEEE Transactions on Consumer Electronics, IEEE Power Engineering Letters, IEEE Access, IEEE Open Access Journal of Power and Energy, CSEE Journal of Power and Energy Systems, Protection and Control of Modern Power Systems, Journal of Modern Power Systems and Clean Energy and Advances in Applied Energy.